Lattice softening significantly reduces thermal conductivity and leads to high thermoelectric efficiency

Riley Hanus[1], Matthias T. Agne[1], Alexander J. E. Rettie[2], Zhiwei Chen[3], Gangjian Tan[4,5], Duck Young Chung[2], Mercouri G. Kanatzidis[2,4], Yanzhong Pei[3], Peter W. Voorhees[1], and G. Jeffrey Snyder[1*]

[1]Materials Science and Engineering, Northwestern University, Evanston, IL 60208, USA.
[2]Materials Science Division, Argonne National Laboratory, Argonne, IL 60439, USA.
[3]Materials Science and Engineering, Tongji University, 4800 Caoan Road, Shanghai 201804, China.
[4]Department of Chemistry, Northwestern University, Evanston, IL 60208, USA.
[5]State Key Laboratory of Advanced Technology for Materials Synthesis and Processing, Wuhan University of Technology, Wuhan 430070, China.
[*]corresponding author, jeff.snyder@northwestern.edu

Abstract

The influence of micro/nanostructure on thermal conductivity is a topic of great scientific interest and of particular technological importance to thermoelectrics. The current understanding is that structural defects primarily decrease thermal conductivity through phonon scattering where the phonon dispersion and speed of sound are fixed when describing thermal transport, especially when chemical composition is unchanged. Experimental work on a PbTe model system is presented which shows that the speed of sound linearly decreases with increased internal-strain. This softening of the materials lattice completely accounts for the reduction in lattice thermal conductivity, without the introduction of additional phonon scattering mechanisms. Additionally, we show that a major contribution to the reduction in thermal conductivity, and the resulting improvement in thermoelectric figure of merit ($zT > 2$), in high efficiency Na-doped PbTe can be attributed to this internal-strain induced lattice softening effect. While inhomogeneous internal-strain fields are known to introduce phonon scattering centers, this study demonstrates that internal-strain can also soften a materials lattice on average, modifying the speeds of sound and phonon dispersion. This presents new avenues to control lattice thermal conductivity, beyond phonon scattering, with microstructural defects and internal-strain. In practice, many engineering materials will exhibit both softening and scattering effects, as is shown in silicon. This work shines new light on studies of thermal conductivity in fields of energy materials, microelectronics, and nano-scale heat transfer.

1 Introduction

Pushing the thermoelectric figure of merit beyond two ($zT > 2$), has been a milestone achievement in the field of energy science. In PbTe, this high zT has been achieved by significantly reducing the lattice thermal conductivity (κ_{L}) at high temperatures [1, 2] (Figure 1a and b). The reduction of κ_{L} in PbTe, and many other thermoelectric and systems, has been realized by controlling the materials micro/nanostructure. This reduced κ_{L} has been rationalized by assuming the lattice defects introduce

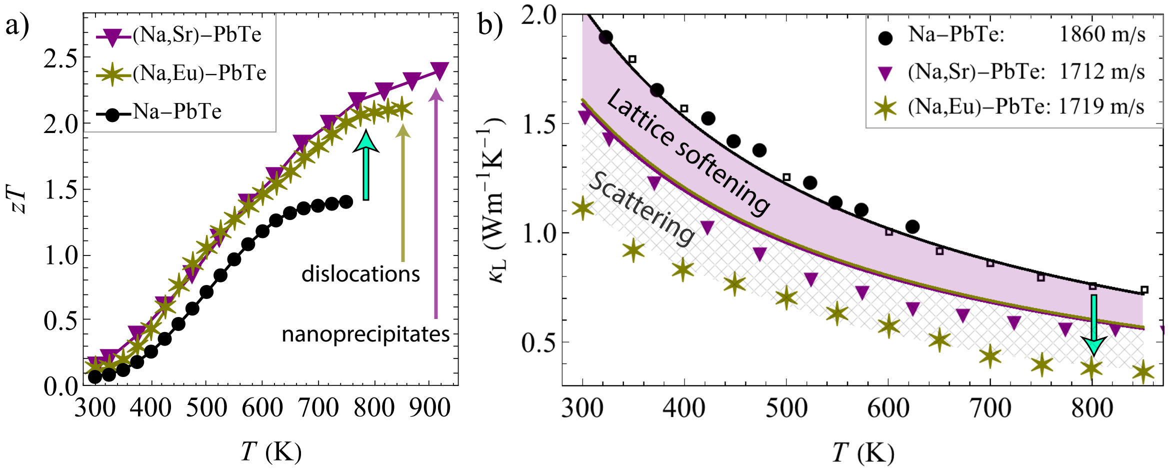

Figure 1: Milestone improvements in the figure of merit (zT) of Na-doped PbTe due to reductions in lattice thermal conductivity (κ_{L}) (a) The improved zT was previously attributed solely to phonon scattering from micro/nanostructural defects. Data for (Na,Sr)-PbTe ($Pb_{0.98}Na_{0.02}Te$-10%SrTe) are from [1], (Na,Eu)-PbTe ($Na_{0.025}Eu_{0.03}Pb_{0.945}Te$) from [2], and Na-PbTe from [3]. (b) A reduction of κ_{L} upon the introduction of micro/nanostructural defects. The lines show the $\kappa_{\mathrm{L}} = Av_{\mathrm{s}}^3T^{-1}$ model describing phonon thermal conductivity in the high-T limit where the only scattering mechanism is phonon-phonon scattering. A is normalized to the Na-PbTe sample and fixed. The shaded region shows the reduction in κ_{L} expected from lattice softening alone, without assuming an increase in phonon-defect scattering centers. Phonon scattering mechanisms could account for the remaining reduction in κ_{L}, depicted by the cross-hatched region. The speed of sound (v_{s}) reduction, measured in this study, is given in the legend. The circles are data for a Na-doped (0.75% Na) sample synthesized and measured in this study. The square data points are a low dislocation density sample from Ref. [4] ($Na_{0.015}Eu_{0.03}Pb_{0.955}Te$).

additional scattering centers which reduces the phonon mean free path (and relaxation time) while the speeds of sound and phonon dispersion are assumed to be fixed (present authors included). However, κ_{L} is very sensitive to changes in the phonon dispersion and thus a materials speed of sound (v_{s}). This can be demonstrated by considering a spectral analysis of the phonon thermal conductivity [5]

$$\kappa_{\mathrm{L}} = \frac{1}{3}\int_{0}^{\omega_{\mathrm{max}}} C_{\mathrm{s}}\, v_{\mathrm{g}}^2\, \tau\, d\omega, \tag{1}$$

where C_{s} is the spectral heat capacity, v_{g} is the group velocity, and τ is the phonon relaxation time. At high temperatures ($T > \theta_{\mathrm{D}}$), when phonon-phonon scattering dominates ($\tau = \tau_{\mathrm{pp}}$) Eq. 1 becomes (details given in Section S1) [6, 7]

$$\kappa_{\mathrm{L}} = \frac{(6\pi^2)^{2/3}\bar{M}}{V^{2/3}4\pi^2\gamma^2}\frac{\langle v_{\mathrm{g}}^3\rangle}{T} = A\frac{v_{\mathrm{s}}^3}{T}. \tag{2}$$

This simple expression produces the same results as the spectral Callaway model (Eqs. 1, S1) when $T > \theta_{\mathrm{D}}$ and $\tau = \tau_{\mathrm{pp}}$ (Eq. S3), and is consistent with the model used by Tan *et al.* [8]. We express it this way to demonstrate the sensitivity of κ_{L} on lattices stiffness which is reflected in the cubic dependence

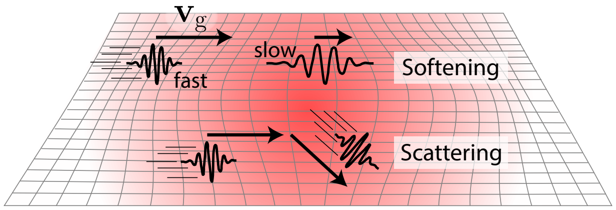

Figure 2: Illustration of phonon scattering and lattice softening effects due to internal-strain fields. The arrows designate the phonon group velocity vector ($\mathbf{v}_{\mathrm{g}}$) for each phonon wave packet (illustrated in the time domain). Internal-strain fields locally change the phonon frequency. This causes both a change the phonon speed as well as introduces phonon scattering centers. Lattice softening refers to a decrease in the phonon speed, the magnitude of the group velocity vector. Phonon scattering refers to a change in the direction of the phonon velocity vector while the phonon speed is unchanged. In order for phonon-defect scattering to be effective at reducing the thermal conductivity it must compete with other scattering mechanisms, such as intrinsic phonon-phonon scattering. Lattice softening is effective regardless of the dominate scattering mechanism.

of κ_{L} on phonon velocity. We denote the average group velocity over the Brilluon zone as $\left\langle v_{\mathrm{g}}^3 \right\rangle$ which is defined in Eq. S5. Additionally, we consolidate the numerical constant and factors of the average atomic mass $\bar{M}$, atomic volume V, and Grüneisen parameter γ into the coefficient A. In practice, A will be normalized to a pristine (control) sample and the change in speed of sound will be used as an estimate for the change in average group velocity ($\left\langle v_{\mathrm{g}}^3 \right\rangle \propto v_{\mathrm{s}}^3$). Thus, if the speed of sound (i.e. lattice stiffness) can be engineered in a material it is expected to be an effective parameter for controlling κ_{L}. In fact, tuning the lattice stiffness is expected to have a larger impact on κ_{L} than micro/nanostructural scattering in some cases. Specifically, at high temperatures, when phonon-defect scattering in anharmonic materials is competing with an intrinsic phonon-phonon mean free path which is already very short. For example, 75% of the heat in intrinsic PbTe is carried by phonons with a mean free path less than approximately $10\,\mathrm{nm}$ (at room temperature), compared to $1000\,\mathrm{nm}$ (at room temperature) for Si [9]. This means only lattice defects that are spaced on the order of $10\,\mathrm{nm}$ should significantly influence κ_{L} in PbTe [10], and this length decreases with increasing temperature.

Internal-strain fields, which are induced by lattice defects such as dislocations and nanoprecipitates, will locally change phonon frequencies within the material and can, in principle, lead to lattice softening. This simultaneously changes phonon speed and induces phonon scattering. The two distinctly different effects are illustrated in Figure 2. Again, the importance of each effect on the lattice thermal conductivity depends on intrinsic material properties and the nature (e.g. length scale) of the internal-strain fields. Specifically, when phonon-phonon scattering is strong (in anharmonic materials and at high temperatures) phonon-strain field scattering is expected to be less important and lattice softening is expected to dominate. Therefore, lattice softening provides a promising avenue for engineering the high temperature thermal conductivity of anharmonic materials, such as thermoelectrics.

Several cases have been presented where an improvement in thermoelectric efficiency is attributed to chemical lattice softening due to alloying or the introduction of vacancies [8, 11]. Additionally, there has been much discussion about the connection between the chemical bonding, and a materials intrinsic lattice stiffness and anharmonicity [12]. Due to the unique bonding characteristics of IV-VI compounds, such as PbTe, they are likely sensitive to the introduction of microstructural defects and in particular lattice strain.

Here, we show a different lattice softening effect where the speed of sound is engineered in stoichiometric PbTe, by changing the amount of internal-strain induced by lattice defects. Astonishingly, in PbTe the observed reduction in speed of sound completely accounts for the reduced κ_{L}. Additionally, internal-strain induced lattice softening is shown to be a major reason for the reduced κ_{L} in high efficiency ($zT > 2$) compositions of Na-doped PbTe [1, 2]. Establishing internal-strain softening as a mechanism for engineering thermal conductivity is not only of critical importance to the field of thermoelectrics, but is also valuable to the fields of nanoscale heat transfer [13], microelectronics [14, 15], and thermal barrier coatings [16, 17].

2 Results

2.1 Lattice softening and thermal conductivity of PbTe

To determine the influence of microstructure and internal-strain on thermal conductivity, stoichiometric PbTe samples were synthesized with varying amounts of internal-strain induced by high energy ball milling (Section 4.1). The low Debye temperature of PbTe ($\theta_{\mathrm{D}} = 150\,\mathrm{K}$) means that room temperature measurements are within the 'high temperature' limit and Eq. 2 is applicable. Since the focus of this study is the lattice thermal conductivity (κ_{L}), the samples were left undoped and were analyzed at temperatures where bipolar effects are negligible (below 400 K). The electronic contributions to the total thermal conductivity were found to be less than 1% of the total (i.e., $\kappa \simeq \kappa_{\mathrm{L}}$). The internal-strain of each pellet sample was measured via XRD peak broadening by the Williamson-Hall method (Section 4.2). The thermal and elastic properties of each pellet were measured by the laser flash method (Section 4.4) and pulse-echo ultrasound (Section 4.3), respectively. The time delay between ultrasound reflections was accurately determined via the maximization of the cross-correlation such that the largest source of error was the measurement of the sample thickness [18]. The error of the pulse-echo measurement was determined to be approximately 1%.

Bulk PbTe pellets containing increasing amounts of internal-strain showed significantly decreased speeds of sound, and this lattice softening was found to completely account for the observed reductions in κ_{L} (Figure 3). Quantitatively, we use Eq. 2 and normalize the coefficient A to the nominally un-strained sample (green squares in Figure 3). This value, $A = 1.09 \times 10^{-7}\,\mathrm{Ws^3m^{-4}}$, is held constant so that v_{s} is the deciding parameter of the model. Thus, since v_{s} is a measurable, there are no free parameters in this model when A is held constant. We note that the experimentally determined value of A is within a factor of three of the theoretical value found for PbTe ($A = 2.6 \times 10^{-7}\,\mathrm{Ws^3m^{-4}}$) which is comparable to models used to predict κ_{L} with semi-emperical models or even *ab intio* calculations [19, 20].

The reduction in κ_{L} measured in these samples can be completely accounted for by lattice softening effects alone (see Eq. 2 and Fig. 3a and b). It is important to recognize that small changes in v_{s}

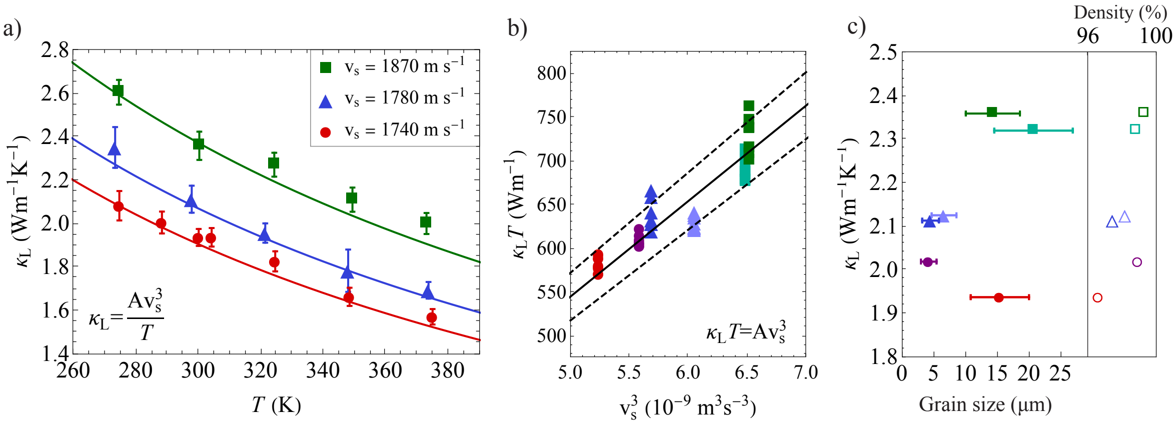

Figure 3: Lattice thermal conductivity of PbTe samples with different amounts of internal strain and average speeds of sound (v_s). (a) κ_L vs. T of three characteristic samples. The lines are applications of the $\kappa_L = Av_s^3T^{-1}$ model where, since the coefficient $A = 1.09 \times 10^{-7} \mathrm{Ws^3m^{-4}}$ is normalized to the unstrained sample (squares) and held constant, there are no adjustable parameters and only difference in the model between samples is the measured v_s. (b) A different representation of Eq. 2, showing the data in panel (a) in comparison to a reproducibility study containing three independently synthesized samples (Figure S4). The dashed lines show a 5% error in κ_L. This data shows that the reduction in lattice thermal conductivity in stoichiometric PbTe is fully accounted for by lattice softening. (c) The measured grain size (filled data points) and density (empty data points) of each sample versus its room temperature κ_L showing that all samples have a density between 97 and 99% of the theoretical density, are large grained, and that there is no systematic trend of κ_L with grain size or density.

correspond to large changes in κ_L. For example, the 7% reduction in v_s observed in stoichiometric PbTe results in a 20% reduction in κ_L, without introducing additional scattering parameters.

To verify the $\kappa_L \propto v_s^3$ relationship, a second series of samples were synthesized and measured, and the results are displayed in Figure 3b, 3c, and S4. The agreement between this reproducibility study and the primary study is shown in Figure 3b. Care was taken to ensure that there was no systematic relationship between κ_L and grain size or density. Figure 3c shows that all sample had a density above 97% of the theoretical density (confirmed by both the geometric and Archemedes method), and that there is no systematic trend of κ_L with grain size measured via scanning electron microscopy (Figure S3). Since the speed of sound measured ultrasonically is sensitive to sample density, the lattice softening measured was confirmed by low-T heat capacity measurements and is shown in Figure S5. The 10% reduction in the Debye temperature, $\theta_D \propto v_s$, is in excellent agreement with the 7% reduction of v_s measured via ultrasound.

2.2 Elastic softening and internal strain

The reductions in speed of sound and lattice thermal conductivity correspond to an increase in internal-strain. As can be seen in Figure 4, the speed of sound decreases linearly with an increase in internal-strain measured via XRD peak broadening. The open diamond data point corresponds to the isotropic average speed of sound of PbTe calculated from the components of the elastic tensor measured on a single crystal [21, 22], and shows this linear trend of v_s extends down to zero internal strain.

Figure 4a shows the measurement of internal-strain of the pellet samples by Williamson-Hall analysis of XRD peak broadening. β is the broadening (integral breadth) of the diffraction peak at angle θ after correcting for instrument broadening. Figure 4b shows the peak fits of samples containing small and large amounts of internal strain. Peak shape asymmetry can be observed, particularly in samples with large amounts of internal strain, where the peak broadening is more significant on the low 2θ (larger d-spacing) side of the peak maximum. This indicates that the state of inhomogeneous internal-strain of these samples has a tendency to increase the lattice plane spacing distribution. An increase in lattice plane spacing (d-spacing) most commonly corresponds to a decrease in phonon frequencies and speeds of sound through considerations of the Grüneisen tensor [23, 24]. From a chemical perspective, bond stiffness is inversely proportional to bond length. A number of extended lattice defects are known to cause peak shape assymetry, including dislocations and coherency strains [25].

The slope of the plots shown in Figure 4a is a measure of $C\epsilon_{\mathrm{XRD}}$, where ϵ_{XRD} is the internal strain determined via the Williamson-Hall method, and C is a constant related to the nature of the strain and details of the analysis method [26, 27, 28]. The full peak broadening analysis, given in Section 4.2, shows that the strain state of the PbTe samples is consistent with dislocations having Burger's vectors in the $\langle 110 \rangle$ direction [29], in agreement with the analysis of Chen *et al.* [4]. Since the spot size of the X-ray beam is approximately $10\,\mathrm{mm}^2$, this method for characterizing strain is a bulk measurement. While transmission electron microscopy provides detailed strain information about specific defects it is limited to small a field of view and is often limited to nanoscale observations. While grain boundaries and interfaces can be a means to introduce internal strain, they do not appear to be the primary cause of internal-strain in the stoichiometric PbTe system (Figure 3c and Figure 4).

The present study also characterized the speed of sound and internal-strain of the $zT > 2$ samples shown in Figure 1 reported by Tan *et al.* [1] and Chen *et al.* [2]. Remarkably, these measurements follow the same trend as that measured in stoichiometric PbTe synthesized for this study (Figure 4). These data indicate that the same softening mechanism observed in the stoichiometric PbTe samples of this study is also present in the high-zT (Na,Eu)-PbTe and (Na,Sr)-PbTe systems. The measured v_{s} in these two samples suggests that a large percentage of the reduction in κ_{L} is due to lattice softening alone (Figure 1b).

The relationship between strain and phonon frequency (and thus the speed of sound) is described through the Grüneisen tensor [23, 24]

$$\gamma_{ij} = -\frac{d\ln\omega}{d\epsilon_{ij}}, \tag{3}$$

which at small strains can be written as

$$\omega = \omega_0(1 - \gamma_{ij}\epsilon_{ij}), \tag{4}$$

where ω_0 is the phonon frequency at zero strain. Recognizing that $\omega \propto v_{\mathrm{s}}$ at low ω, it is possible to define an engineering Grüneisen parameter γ_{int}, which is associated with the internal-strain state of PbTe measured via XRD. Then,

$$v_{\mathrm{s}} = v_{\mathrm{s},0}\left(1 - \gamma_{\mathrm{int}}\epsilon_{\mathrm{XRD}}\right). \tag{5}$$

This expression is consistent with the experimental observation of a linear dependence of speed of sound on strain. From a fit of Eq. 5 to the experimental data in Figure 4c using $C = 4$ [28, 27, 26], we estimate that $\gamma_{\mathrm{int}} = 5$, which similar to the thermodynamic Grüneisen parameter of PbTe ($\gamma = 2.2$, Ref. [21]). The order of magnitude agreement between γ_{int} and γ for PbTe strongly supports the argument that internal-strain is the origin of lattice softening, reduced κ_{L} and improved zT. It should be noted that the analysis shown in Figure 4a determines relative changes in internal-strain, and that the absolute magnitude of internal strain depends on the value of C. Thus, γ_{int} is an experimental parameter that is expected to be consistent when the analysis method is consistent between samples. Several other theories predict softening with increasing strain and/or dislocation density [30, 31, 32, 33]. Theories that relate lattice softening explicitly to strain energy give a quadratic dependence on strain, rather than the linear dependence observed in this study [31, 32, 33].

3 Discussion

3.1 Temperature dependence of κ_{L} reduction: scattering vs. softening

Lattice softening is fundamentally different than phonon-defect scattering as a mechanism to reduce κ_{L}. Thus, softening and defect scattering have distinguishing features in the temperature dependence of κ_{L}. This difference stems from the fact that phonon-phonon scattering has a $\tau_{\mathrm{pp}}^{-1} \propto T$ temperature dependence above the Debye temperature, whereas all elastic phonon-defect scattering mechanisms (τ_{defect}) are independent of temperature, given that the defect concentration is approximately constant with temperature (Table I of Klemens [34]). Consequently, phonon-defect scattering should be proportionally more effective at lower temperatures than at higher temperatures. Lattice softening is effective at all temperatures since it reduces thermal conductivity regardless of scattering mechanisms. This is demonstrated in the schematic model shown in Figure 5, which is based on Eqs. 1, S1, and S3. The black line indicates a pristine sample with speed of sound $v_{\mathrm{s},1}$ (e.g. a single crystal, or nominally unstrained and large grained polycrystal). The dashed line represents a defective material where the speed of sound stays constant at $v_{\mathrm{s},1}$ and κ_{L} is reduced by defect scattering (i.e. temperature independent τ_{defect}). The dark red line illustrates a reduction in κ_{L} through lattice softening (i.e. a reduction in speed of sound, $v_{\mathrm{s},2} < v_{\mathrm{s},1}$) without changing scattering mechanisms. When analyzing thermal conductivity as κ_{L} vs. T (as in Figure 5a) it may be difficult to determine if scattering or softening is the primary mechanism of κ_{L} reduction. However the difference in the temperature dependence can be more clearly seen by normalizing the thermal conductivity of the defective sample by that of the pristine sample ($\kappa/\kappa_{\mathrm{o}}$). A positive slope of $\kappa/\kappa_{\mathrm{o}}$ with temperature is characteristic of phonon-defect scattering. In contradistinction, if lattice softening dominates, $\kappa/\kappa_{\mathrm{o}}$ is expected to be constant with temperature (Figure 5b). To verify lattice softening effects are present, elasticity, low-T heat capacity, and/or phonon density of states measurements are required.

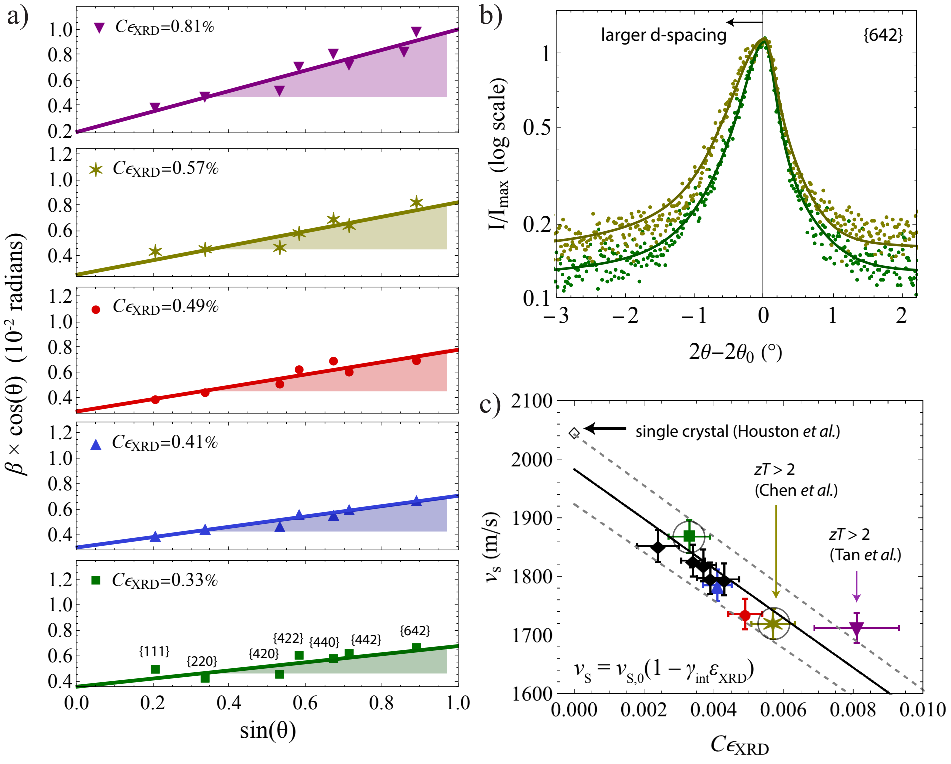

Figure 4: Speed of sound decreases linearly with increasing internal-strain in PbTe based materials. a) Williamson-Hall strain analysis of stoichiometric PbTe, as well as Na-doped, high zT, compositions (colors are consistent with Figure 1 and 3). β is the integral breadth (peak area/height) of a diffraction peak at θ. The slope of the plots ($C\epsilon_{\mathrm{XRD}}$) are proportional to the average internal-strain in the material (details in Section 4.2). b) Example peak fits of a low and high internal-strain samples (circled in panel (c)). Diffraction peaks in samples with large amounts of internal-strain show peak shape asymmetry where the peak has a larger broadening on the low 2θ (larger d-spacing) side of the peak maximum. c) The speed of sound (v_{s}) measured by pulse-echo ultrasound versus the internal-strain ($C\epsilon_{\mathrm{XRD}}$) as measured in panel (a). The increase in internal-strain is correlated with a linear decrease in the speed of sound, a reduction in the lattice thermal conductivity, and improved thermoelectric efficiency.

Lattice softening has been observed by low-T heat capacity in Si, where the measured v_{s} reduces from $5830\,\mathrm{m\ s^{-1}}$ in a Si single crystal [35] and $5700\,\mathrm{m\ s^{-1}}$ in a polycrystal, to $4440\,\mathrm{m\ s^{-1}}$ in a nanocrystalline material [36]. However, the phonon-phonon mean free path in Si is large at room temperature, with 75% of the heat being transported with a mean free path ($\Lambda = v_{\mathrm{g}}\tau$) larger than approximately $100\,\mathrm{nm}$. Therefore, nanocyrstalline Si is still expected to have significant phonon scattering effects at room temperature due to grain boundary scattering. Figure 6a shows the lattice thermal conductivity of single crystal [37] and nanocrystalline Si with an average grain size of $42\,\mathrm{nm}$ [36]. The lines show a transport model constructed to estimate the relative importance of lattice softening and phonon-scattering in this system. This Callaway-type model has been used previously for Si [38, 39], but did not consider changes in speed of sound. In these studies, τ_{pp} is calibrated to single crystalline data and fixed. Here, τ_{pp} is parameterized to capture the experimentally observed lattice softening effects, such that the explicit dependence of τ_{pp} on the phonon velocity is left intact (Eq. 11). In the previous studies [38, 39],

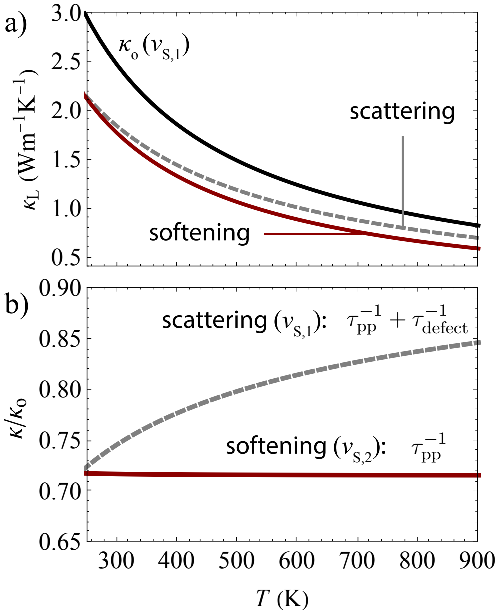

Figure 5: A schematic model transport model demonstrating the characteristics features of defect scattering and lattice softening mechanisms in the reduction of lattice thermal conductivity (κ_{L}). a) The κ_{L} of a pristine sample (κ_{o}) compared the κ_{L} of defective samples where the reduction in κ_{L} is induced by phonon-defect scattering and lattice softening. In the pristine sample (κ_{o}), and the case of lattice softening (dark red), $\tau^{-1} = \tau_{\mathrm{pp}}^{-1} \propto T$. For the case of phonon-defect scattering (dashed), $\tau^{-1} = \tau_{\mathrm{pp}}^{-1} + \tau_{\mathrm{defect}}^{-1} \propto T + \mathrm{constant}$. b) The ratio of κ_{L} for the defective sample over that for the pristine sample. A positive slope of $\kappa/\kappa_{\mathrm{o}}$ indicates significant phonon scattering effects, and no slope indicates softening effects.

this dependence was buried in the numerical constants. Thus, the model used herein is able to capture lattice softening effects. It is not surprising, then, that the 24% reduction in v_{s} going from single- to nano-crystalline Si coincides with a large predicted reduction in κ_{L} (red shaded region in Fig. 6a). To account for grain boundary scattering in the nanocrystalline material, the relaxation time due to phonon interactions with lattice rotation and localized strain fields at grain boundaries (τ_{gbs}) is applied [39]. All parameters associated with the nanoscale structure of the grain boundaries are fixed to those that were used in the low-T κ_{L} model in Ref. [39], and the grain size was set to $42\,\mathrm{nm}$, which was measured experimentally [36]. Therefore, the model captures the entire reduction of κ_{L} from single- to nano-crystalline samples using experimentally measured speed of sound and grain size, without any additional fitting parameters (black and teal lines in Figure 6a). This model indicates that at room temperature, phonon-grain boundary scattering and lattice softening are equally important, whereas at high temperatures ($> 1000\,\mathrm{K}$) lattice softening dominates. The dashed line shows a predicted κ_{L} if lattice softening is not included. Phonon scattering on point impurities and free charge carriers in the Si-nc were determined to be negligible and are discussed in Section 4.6.

In Figure 6b and c, we show the κ_{L} of the defective samples normalized by that of the pristine sample (Si single crystal, and large grain unstrained Na-PbTe). Indeed, a positive slope in $\kappa/\kappa_{\mathrm{o}}$ vs. T is observed in Si near room temperature, where significant scattering is present (compare to Figure 5b). In PbTe, however, $\kappa/\kappa_{\mathrm{o}}$ vs. T is relatively flat which is consistent with the lattice softening measured in Figure

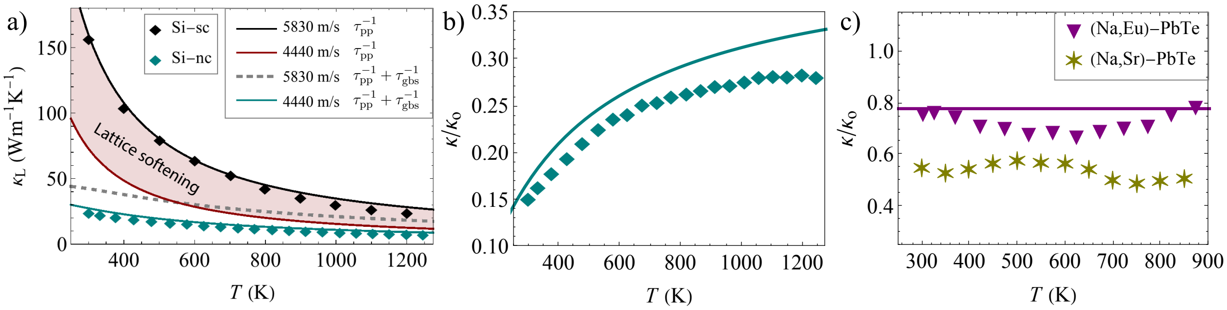

Figure 6: The temperature dependent reduction of lattice thermal conductivity ($\kappa_{\rm L}$) in Si and PbTe. a) A Callaway-type thermal transport model used to estimate the effects of lattice softening and phonon-grain boundary scattering in reducing $\kappa_{\rm L}$ from single cyrstal (sc, [37]) to nanocrystalline (nc, [36]) Si, with average grain size of $42\,{\rm nm}$. The red shaded region shows the reduction in lattice thermal conductivity expected from measured lattice softening alone. Phonon-grain boundary scattering was included using the expression derived by Hanus *et al.* [39], $\tau_{\rm gbs}$, where the only parameter changed from Ref. [39] to this study is the grain size. Therefore, the only parameters in the model changed from Si-sc to Si-nc are the experimentally measured $v_{\rm s}$ and grain size. The dashed line shows the predicted $\kappa_{\rm L}$ if lattice softening is not included. b) The normalized $\kappa_{\rm L}$ of Si-nc showing a positive slope with T around room temperature indicates phonon scattering effects are important. c) The normalized $\kappa_{\rm L}$ of high-zT Na-doped PbTe samples showing a flat temperature dependence indicating that lattice softening is important.

4. This analysis of Si and PbTe demonstrates that lattice softening and scattering effects can both contribute to the reduction of $\kappa_{\rm L}$ in engineering materials. However, the relative contribution of each effect depends on the specific material and microstructure. Here, it is shown that lattice softening can account for over 50% of the reduction in $\kappa_{\rm L}$, and is consequently a primary mechanism with which to engineer thermal conductivity.

3.2 The connection between speed of sound and heat carrying phonons

The speed of sound is a measure of the slope of the phonon dispersion relation near the center of the Brillouin zone (Γ-point). Acoustic measurements of speed of sound and elastic properties are typically made in the kHz to MHz frequency range. Measurement of the speed of sound at higher frequencies can be obtained from the Debye level found from low-T heat capacity ($\approx 10^2$ GHz) or phonon density of states (≈ 1 THz). Phonons which carry significant amounts of heat are in the THz frequnecy range. Thus, measurements of speed of sound are not typically made directly on heat carrying phonons. However, speed of sound is inherently a measurement of bond stiffness which is governed by the interatomic force constants.

Interatomic force constants simultaneously govern the speed of sound as well as the frequency and group velocity of phonons throughout the Brillouin zone [24]. Consequently, acoustic measurements can be used as a gauge for the general behavior of the full phonon dispersion. One justification for this is that the speed of sound has been shown to be an accurate predictor for the average phonon frequency across material systems [40]. Additionally, it is known that Raman-active optical modes typically have a linear strain dependence that can also be characterized by a Gruneisen parameter [41, 42]. From theoretical considerations, this optical Gruneisen parameter is ≈ 6.5 for ionic materials and ≈ 3 for covalently bonded materials [42]. The phonon mode dependent Grüneisen parameter has been computed for PbTe and values for the optical branches are of similar sign and magnitude [43]. The thermal conductivity of homogeneously strained PbTe has also been computed by Murphy et al. [44]. The results show that positive tensile strain, indeed, strongly reduced the transverse optical Γ-point frequency and the magnitude of reduction in κ_{L} with increasing strain generally agrees with the experimental results presented here. Therefore, speed of sound measurements are very useful in probing the bond stiffness and in turn the general behavior of heat carrying phonons in defective systems where direct measurement or calculation of THz phonons is prohibitively difficult or impossible (e.g. polycrystalline and heavily strained materials).

3.3 Engineering thermal conductivity through lattice softening

Internal-strain induced lattice softening has been demonstrated as a promising method to reduce thermal conductivity. Therefore, methods of introducing and maintaining large amounts of internal-strain should be considered, rather than methods which increase the spacial density of defects, particularly in anharmonic materials. The PbTe study presented here utilized high-energy ball milling in conjunction with a rapid hot-pressing procedure developed to minimize the annealling out of internal-strain. Other processing techniques such as high pressure torsion [45], hot deformation [46], and liquid phase sintering [47] may be optimized to maximize the amount of internal-strain in the material. The softening effects in Si and Si-Ge alloys by Caudio *et al.* [36, 48], and in $\mathrm{Bi_2Te_3}$ and $\mathrm{Sb_2Te_3}$ based materials by Klobes *et al.* [49] were seen with decreasing grain size. While decreasing grain size often correlates with an increased amount of internal-strain, this is not always the case (as we show in Figures 3 and 4). Nevertheless, given that microstructural defects contribute to both lattice softening and scattering, it is no surprise that good thermoelectric materials with low thermal conductivity are highly defective. However, lattice softening is a particularly promising avenue for thermoelectrics as it allows for a reduction in κ_{L} without the requirement of a large spacial density of defects which likely induce electron scattering as well.

It is also possible to induce lattice softening through chemical methods. Recently, we reported a speed of sound reduction when alloying SnTe with $\mathrm{AgSbTe_2}$ which is required to explain the dramatic reduction in lattice thermal conductivity and improvement in zT [8]. Again, the transport model only quantitatively agrees with experiment if the speed of sound is monitored throughout the study. Beyond semiconductors, lattice softening has been measured in metallic [31] and ionic materials [50] with increased point defect concentrations. The magnitude of such effects could be assessed with similar experimental methods as those presented here. The totality of these reports indicates that elastic softening should be important in many engineering materials other than PbTe. It is interesting to note that the internal-strain softening effect described here may even be taken to the limit of amorphous materials, which have been theoretically described as fully defective crystals, and whose elastic moduli are nearly universally lower than there crystalline analogues [51].

4 Methods

4.1 Synthesis

Ingots (between 20 to 40 g) of nominally stoichiometric PbTe were prepared from elemental Pb (Alfa Aesar, lead rod, $6.35\,\mathrm{mm}$ diameter, 99.999%) and Te (Alfa Aesar, Tellurium lump, 99.999+%) by melt reaction under vacuum ($\sim 10^{-4}\,\mathrm{torr}$) in a carbon-coated quartz ampule (12 mm inside diameter x 16 mm outside diameter) at $1000\,^{\circ}\mathrm{C}$ for 4 to 6 hours and quenched in ice water. Each ingot was independently pulverized by mortar and pestle and sieved to have an initial particle size distribution between 20 to $120\,\mu\mathrm{m}$. This material was considered to be nominally un-strained. Plastic deformation was introduced via high-energy ball milling for varying durations (5 to $120\,\mathrm{min}$). The ball milling process was standardized such that $2.0\,\mathrm{g}$ of unstrained powder was loaded into a stainless steel jar (with inner dimensions of $36.7\,\mathrm{mm}$ in diameter and $57\,\mathrm{mm}$ in height) along with the same size and number of grinding media (2 stainless steel balls $12.7\,\mathrm{mm}$ in diameter and 15 stainless steel balls $6.3\,\mathrm{mm}$ in diameter) and sealed in an argon atmosphere. All powders were consolidated by uniaxially hot pressing in a high density graphite die under argon atmosphere. The maximum pressure of $\sim 45\,\mathrm{MPa}$ and maximum temperature of $550\,^{\circ}\mathrm{C}$ were held concurrently for $20\,\mathrm{min}$. As the temperature ramped from room temperature to $550\,^{\circ}\mathrm{C}$, the pressure was applied stepwise in $10\,\mathrm{MPa}$ intervals. Both temperature and pressure reached their maximum value in $10\,\mathrm{min}$. After consolidating for $20\,\mathrm{min}$, the samples were furnace cooled under a nominal pressure of $5\,\mathrm{MPa}$. All pellets had a density $> 97\%$ theoretical density ($8.16\,\mathrm{g\,cm^{-3}}$), measured by both geometric and Archimedes methods. To minimize error introduced in speed of sound and thermal diffusivity measurements, all samples were sanded and polished to be parallel such that the thickness variation was within 1% of the mean, measured with a micrometer.

Figure S1 shows the internal-strain (measurement described in Section 4.2) as a function of high energy ball milling time. The amount of internal-strain induced during ball milling can vary with many experimental factors. We found that if the initial particle size distribution is controlled by sieving, the amount of powder being ball milled is kept constant, as well as the milling media and size of the ball milling vial, the internal-strain versus ball milling time trend can be reproduced within experimental uncertainty, as can be seen by comparing the two trials in Figure S1a.

Figure S1b shows the variability seen if all of the mentioned experimental parameters are not controlled. Nevertheless, the speeds of sound correlate with measured internal strain regardless of ball milling conditions (Figure 4b).

Figures S1a and b also show that internal-strain increases with ball milling time until a plateau is reached at approximately one to two hours depending on previously mentioned details regarding the ball milling procedure. This type of plateau is commonly observed in powder metallurgy, and is sometimes followed by a decrease in internal strain [52].

4.2 X-Ray diffraction and analysis

4.2.1 X-Ray data collection

X-Ray diffraction was conducted on a STOE STADI-MP with pure Cu K-$\alpha 1$ radiation (Figure S2). Pre-pressed powders were measured in transmission mode (Debye-Scherrer geometry) and pressed pellets were measured in reflection mode (Bragg-Brentano geometry). A NIST 640e silicon standard was used to calibrate the peak position, and NIST 660c LaB_6 standard was used to characterize the instrumental peak broadening. The instrumental broadening is shown in relation to the peak broadening of a typical PbTe sample in the inset of Figure S2a, where the $2\theta = 71.8°$ LaB_6 peak is normalized in intensity and position for comparison to the PbTe peak. This shows that the instrument resolution in peak width is sufficient for particle size and internal-strain analysis. Since strain information is contained primarily in high angle reflections, data was collected up to $2\theta = 110°$ for powders in transmission mode and $2\theta = 130°$ for pellets in reflection, with sufficient counting time to fully resolve the high angle peaks.

4.2.2 Reitveld refinement and evidence of $\langle 110 \rangle$ dislocations

GSAS II was used to conduct Reitveld refinements [53]. An instrument parameter file was constructed in GSAS II by refining the LaB_6 standard, with no sample size or microstrain broadening included. The instrument parameter file was not changed durning refinement of PbTe samples. When refining PbTe ($\mathrm{Fm\bar{3}m}$) samples, the lattice parameter and sample position were first refined separately and then together. Then the particle size was set to its maximum (10μm) and microstrain was refined. Since significant anisotropic peak broadening was observed in all samples (peak width is not a smooth function of θ) the generalized anisotropic strain model was used in GSAS II to describe the internal strain, analogous to that used by Christensen et al. [54] in JANA2006. This model allows for two independent strain parameters, S_{400} and S_{220}, and a typical result is shown as a strain surface plot in Figure S2b. This strain model shows that the crystal is less strained in the principle crystallographic directions, as observed by the 'dimples' along the x, y, and z directions of Figure S2b. Additionally, this is reflected in the raw peak fits shown in Figure S2c, as well as the aniostropic strain parameters in which all samples show, $2S_{400} < S_{220}$. This type of strain state is consistent with that of a dislocation with a Burger's vector in the $\langle 110 \rangle$ direction, as shown in Figure S2d. This dislocation line points into the page and the Burger's vector is rotated $45°$ from the principle directions, such that there is a zero strain node in the σ_{yy} and σ_{xy} components of the stress tensor in the principle crystallographic directions [29]. This data suggests that the dominate defect inducing the internal strain are dislocation with Burger's vector equal to $(a/2)\langle 110 \rangle$, which are known to be the low energy dislocation type in PbTe [29]. Finally, the size was refined separately and then together with strain resulting in no significant contribution to peak broadening from particle size effects. Then all previously refined parameters were refined together (instrument parameters still fixed) and the resulting fit is shown in Figure S2. The reproducibility of internal strain analysis was verified by refining five independent X-ray scans on the same batch of powder. The standard deviation of internal strain measurements had a value that was 3% of the mean. No change in the lattice parameter was measured.

4.2.3 Williamson-Hall peak broadening analysis

To analyze the internal strain of the pressed pellets, select peaks were fit using a split psuedo-Voigt function

$$I(2\theta) = I_{hkl}[\eta\, L(2\theta - 2\theta_0)) + (1-\eta)G(2\theta - 2\theta_0)]. \tag{6}$$

The Lorenzian full width half max (σ) was allowed to be different on the left and right side of the peak maximum,

$$L(2\theta - 2\theta_0) = \frac{(\sigma/2)^2}{(2\theta - 2\theta_0)^2 + (\sigma/2)^2} \cdot \begin{cases} \sigma = \sigma_L\,, & 2\theta \leq 2\theta_0 \\ \sigma = \sigma_R\,, & 2\theta > 2\theta_0 \end{cases} \tag{7}$$

The Gaussian peak shape function is given by

$$G(2\theta - 2\theta_0) = \exp\left(-\frac{\pi(2\theta - 2\theta_0)^2}{\beta_G^2}\right), \tag{8}$$

where β_{G} is the Gaussian peak width. The θ dependence of the peak width was analyzed via the Williamson-Hall method. While the same conclusions can be made by analyzing Reitveld refinement results of the pressed pellets, the Williamson-Hall method was used because it resulted in a lower analysis related error. Additionally, while the results presented in Figure S2 suggest that the primary strain inducing defect is a dislocation with Burger's vector $(a/2)\,\langle 110\rangle$, the Williamson-Hall approach used on the pellets is model *non*-specific and no conclusion about the microscopic origin of the internal strain is required.

Individual peaks were fit using the split pseudo-Voigt profile function (Eq. 6) the integral breadth (area/height) of the fitted peak is given by β_{meas}. The instrument integral breadth, β_{inst} was determined by conducting the same fitting procedure on a NIST 660c LaB$_6$ standard. The sample full width at half maximum was then calculated by $\beta^2 = \beta^2_{\mathrm{meas}} - \beta^2_{\mathrm{inst}}$ and converted from degrees into radians for analysis. The Williamson-Hall function was used to determine the relative amounts of internal strain in each pellet sample

$$\beta \cos\theta = (C\epsilon_{\mathrm{XRD}}) \sin\theta + \frac{\lambda}{d_{\mathrm{XRD}}}\,, \tag{9}$$

where β is the instrument corrected full width half maximum (in radians), θ is the angle of the diffraction peak, λ is the wavelength of the radiation, $C = 4$ is a constant related to the nature of the internal strain [28, 27, 26], and ϵ_{XRD} and d_{XRD} are the internal strain and crystallite domain size determined via this Williamson-Hall method. As can be seen in Figure S2c, the $\{h00\}$ type peaks were significantly sharper than the other peaks [38, 54] and were thus excluded from the Williamson-Hall analysis. The resulting least squares fits are shown as lines in Figures 4a and S2c.

4.3 Pulse-echo ultrasound

The speeds of sound were measured by the pulse-echo method where a piezoelectric transducer coupled to the sample first sends the initial stress-wave pulse, and then acts as receiver measuring the echoed ultrasound reflection [55]. Since no preferred orientation was observed in the X-Ray analysis, the randomly oriented polycrystals were treated as elastically isotropic. The time-delay, t_d, between subsequent reflections was determined by maximizing the cross-correlation of the two reflections as follows. If $A_n(t)$ is the amplitude of reflection n, then $\sum_t A_n(t)A_{n+1}(t-t_\mathrm{d})$ is maximized by varying t_d. This corresponding value of t_d along with the sample thickness, h, was then used to calculate the speed of sound, $v_\mathrm{L,T} = 2h/t_\mathrm{d}$. A longitudinal transducer (measuring v_L) with a principle frequency of 5 MHz (Olympus V1091) and a transverse transducer (measuring v_T) at 5 MHz (Olympus V157-RM) were used with a Panametrics 5072PR pulser/receiver. A Tektronix TBS 1072B-EDU oscilloscope was used to record the waveforms. A typical waveform contained around four reflections (3 time-delay measurements), and the measurements from a minimum of three waveforms (corresponding to 9 individual speed of sound measurements) were averaged. All measurements had a standard deviation of less than 1% of the mean. The largest error in this measurement technique is the measurement of the sample thickness, and if care is taken to ensure the sample faces are parallel and a micrometer is used to measure the sample thickness, $< 1\%$ analysis related error is achievable. A single crystal of yttrium aluminum garnet (YAG) with known elastic properties was used to determine that measurements of the speed of sound on this home built system have an accuracy of better than 0.6%. The average speed of sound is calculated as [56]

$$v_s = \left(\frac{1}{3}\left[\frac{1}{v_L^3} + \frac{2}{v_T^3}\right]\right)^{-1/3} . \tag{10}$$

4.4 Thermal diffusivity and conductivity

Thermal diffusivity was measured using a Netzch laser flash analysis (LFA) system. The diffusivity measurements, D_κ [m^{2}s^{-1}], were combined with the heat capacity of PbTe [3], $c_\mathrm{p}\,[\mathrm{JK^{-1}m^{-3}}] = NR\{3.07 + 4.07 \times 10^{-4}(T-300)\}/M$ (where N is the number of atoms per primitive unit cell, $R\,[\mathrm{J\,K^{-1}mol^{-1}}]$ is the gas constant, and $M\,[\mathrm{kg\,mol^{-1}}]$ is the molar mass of the primitive unit cell), and the sample density, $\rho\,[\mathrm{kg\,m^{-3}}]$, to calculate the thermal conductivity, $\kappa = D_\kappa c_\mathrm{p}\rho\,[\mathrm{Wm^{-1}K^{-1}}]$. Electrical conductivity measurements confirmed that the electronic thermal conductivity is less than 1% of κ, so the thermal conductivity measured is essentially equal to the lattice thermal conductivity, $\kappa \simeq \kappa_L$ (bipolar thermal conduction is negligible in the temperature range considered for undoped PbTe).

4.5 Grain size from SEM

Figure S3 shows scanning electron microscopy (SEM) images of three samples, which were used to determine the grain size via the lineal intercept method [57]. The images were obtained on a Hitachi

S-4800 in the secondary electron mode, with a beam voltage of 2 kV. This method gives an estimate of the grain size which is accurate to approximately 25%.

4.6 Thermal transport model for nanocrystalline Si

The thermal transport model shown Figure 6a is identical to that shown in Figure 2 of Ref. [58] and Figure 8a of Ref. [39] except that the phonon-phonon relaxation time was formulated to maintain its dependence on phonon velocity [7],

$$\frac{1}{\tau_{\mathrm{pp}}(\omega)} = \frac{c_1 \omega^2 T}{v_{\mathrm{s}}^3} e^{-c_2 v_{\mathrm{s}}/T}. \tag{11}$$

The coefficients here are related to the coefficients in Ref. [39] as $C_1 = c_1/v_{\mathrm{s}}^3$ and $C_2 = c_2 v_{\mathrm{s}}$. Phonon-grain boundary scattering was included using the relaxation time derived in Ref. [39] which describes a phonon being perturbed by the grain boundary rotation and localized strain field and is given by

$$\frac{1}{\tau_{\mathrm{gbs}}(\omega)} = A_1\, n_{\mathrm{1d}} v_{\mathrm{s}} \gamma^2 \left(\frac{b}{D}\right)^2 + B_1 \left(\frac{n_{\mathrm{1d}}}{D}\right) \gamma^2 b^2 (\omega - \omega^*) \Theta\left(\omega - \omega^*\right), \tag{12}$$

where

$$\omega^* = \frac{4\pi v_{\mathrm{s}}}{3D}\,, \tag{13}$$

is the dimensionality crossover frequency and $\Theta(x)$ is the Heaviside step function. $A_1 = 8/3$ and $B_1 = 0.93 K_\nu$, where

$$K_\nu = 1 + \frac{(1-2\nu)^2}{4(1-\nu)^2} + \frac{1}{32(1-\nu)^2}. \tag{14}$$

The total relaxation time is calculated according to Matthiessen's Rule: $\tau^{-1} = \tau_{\mathrm{pp}}^{-1} + \tau_{\mathrm{gbs}}^{-1}$.

The speed of sound for a Si single crystal is slightly different here than that used in Ref. [39] because we are utilizing speeds of sound obtained by low-T heat capacity rather than elastic moduli. Intrinsic phonon-point defects scattering (natural vacancies and isotopes), as well extrinsic point defect scattering due to mass contrast and localized strain fields (P substituted on a Si site) were determined to be negligible [59]. From the measured carrier concentration of the nanocyrstalline Si sample [36], the fraction of P on Si sites was only $f = 0.002$, and the mass difference and change in atomic radii of P and Si are relatively small. Additionally, phonons scattering on conduction electrons, which mainly effects low frequency phonons, was neglected since the relaxation time of low frequency phonons is already dominated by phonon GB scattering [60]. The material parameters utilized for the model are shown in Table S2.

5 Conclusion

Here, in a PbTe model system, we experimentally established the importance of lattice softening effects on thermal transport. Significant reductions in the thermal conductivity of polycrystalline PbTe were completely accounted for by reductions in the materials average speed of sound, without invoking additional phonon scattering terms. In nanocrystalline Si, both softening and scattering effects were necessary to describe the thermal conductivity reduction. These results demonstrate that monitoring the elasticity of a material throughout a study is of critical importance.

The reduction in speed of sound is found to be linearly related to the increase in the internal-strain of a material. This can be described by defining an engineering Grüneisen parameter which behaves like a material property of PbTe, $\gamma_{\mathrm{int}} \approx 5$. With this new understanding of lattice softening, and its implications on thermal transport, it is not surprising that materials processing methods which create and maintain large amounts of internal-strain tend to improve thermoelectric efficiency. Or, more specifically, that these methods are effective at reducing the lattice thermal conductivity at high temperatures, even in very anharmonic materials where the intrinsic phonon-phonon mean free path is already very small.

Acknowledgements

RH acknowledges support from the Johannes and Julia Randall Weertman Graduate Fellowship. MTA acknowledges support from the PPG graduate fellowship. GJS and MTA acknowledges thermoelectrics research at Northwestern University through the Center for Hierarchical Materials Design (CHiMaD). RH would like to thank Christos Malliakas for assistance with the X-Ray characterization at IMSERC at Northwestern University, which has received support from the Soft and Hybrid Nanotechnology Experimental (SHyNE) Resource (NSF ECCS-1542205); the State of Illinois and International Institute for Nanotechnology (IIN). This work made use of the EPIC facility of Northwestern University?s NUANCE Center (SEM), which has received support from the Soft and Hybrid Nanotechnology Experimental (SHyNE) Resource (NSF ECCS-1542205); the MRSEC program (NSF DMR-1720139) at the Materials Research Center; the International Institute for Nanotechnology (IIN); the Keck Foundation; and the State of Illinois, through the IIN. YP and ZC acknowledge the financial support from the National Natural Science Foundation of China (Grant No. 11474219 and 51772215). The work in the Materials Science Division of Argonne National Laboratory (low-temperature heat capacity measurements) was supported by the U.S. Department of Energy, Office of Science, Basic Energy Sciences, Materials Sciences and Engineering Division, under contract No. DE-AC02-06CH11357.

Contributions

RH drafted the manuscript. RH, MTA and GJS designed the experiment. RH and MTA conducted the experimental and theoretical work. AR and DYC conducted the low-T heat capacity measurements. ZC and YP synthesized and provided the (Na,Eu)-PbTe sample for characterization. GT and MK synthesized and provided the (Na,Sr)-PbTe sample for characterization. All authors revised and commented on the manuscript.

References

[1] G. Tan, F. Shi, S. Hao, L.-D. Zhao, H. Chi, X. Zhang, C. Uher, C. Wolverton, V. P. Dravid, M. G. Kanatzidis. *Nature Communications* **2016**, *7*, 1 12167.

[2] Z. Chen, Z. Jian, W. Li, Y. Chang, B. Ge, R. Hanus, J. Yang, Y. Chen, M. Huang, G. J. Snyder, Y. Pei. *Advanced Materials* **2017**, *1606768* 1606768.

[3] Y. Pei, A. LaLonde, S. Iwanaga, G. J. Snyder. *Energy and Environmental Science* **2011**, *4*, 6 2085.

[4] Z. Chen, B. Ge, W. Li, S. Lin, J. Shen, Y. Chang, R. Hanus, G. J. Snyder, Y. Pei. *Nature Communications* **2017**, *8* 13828.

[5] M. Kaviany. *Heat Transfer Physics*. Cambridge Universtiy Press, New York, 1st edition, **2008**.

[6] E. S. Toberer, A. Zevalkink, G. J. Snyder. *Journal of Materials Chemistry* **2011**, *21*, 40 15843.

[7] G. A. Slack, S. Galginaitis. *Physical Review* **1964**, *133*, 1A.

[8] G. Tan, S. Hao, R. C. Hanus, X. Zhang, S. Anand, T. P. Bailey, A. J. E. Rettie, X. Su, C. Uher, V. P. Dravid, G. J. Snyder, C. Wolverton, M. G. Kanatzidis. *ACS Energy Letters* **2018**, *3*, 3 705.

[9] Z. Liu, J. Mao, T.-H. Liu, G. Chen, Z. Ren. *MRS Bulletin* **2018**, *43*, 03 181.

[10] Y. K. Koh, C. J. Vineis, S. D. Calawa, M. P. Walsh, D. G. Cahill. *Applied Physics Letters* **2009**, *94*, 15 2007.

[11] S. Y. Back, H. Cho, Y.-K. Kim, S. Byeon, H. Jin, K. Koumoto, J.-S. Rhyee. *AIP Advances* **2018**, *8*, 11 115227.

[12] S. Lee, K. Esfarjani, T. Luo, J. Zhou, Z. Tian, G. Chen. *Nature communications* **2014**, *5* 3525.

[13] D. G. Cahill, P. V. Braun, G. Chen, D. R. Clarke, S. Fan, K. E. Goodson, P. Keblinski, W. P. King, G. D. Mahan, A. Majumdar, H. J. Maris, S. R. Phillpot, E. Pop, L. Shi. *Applied Physics Reviews* **2014**, *1*, 1 1.

[14] E. Pop. *Nano Research* **2010**, *3*, 3 147.

[15] C. Mion, J. F. Muth, E. A. Preble, D. Hanser. *Applied Physics Letters* **2006**, *89*, 9.

[16] D. R. Clarke. *Surface and Coatings Technology* **2003**, *163-164* 67.

[17] H. S. Yang, G. R. Bai, L. J. Thompson, J. a. Eastman. *Acta Materialia* **2002**, *50*, 9 2309.

[18] C. Pantea, D. G. Rickel, A. Migliori, R. G. Leisure, J. Zhang, Y. Zhao, S. El-Khatib, B. Li. *Review of Scientific Instruments* **2005**, *76*, 11 114902.

[19] C. Toher, J. J. Plata, O. Levy, M. de Jong, M. Asta, M. B. Nardelli, S. Curtarolo. *Physical Review B* **2014**, *90*, 17 174107.

[20] S. A. Miller, P. Gorai, B. R. Ortiz, A. Goyal, D. Gao, S. A. Barnett, T. O. Mason, G. J. Snyder, Q. Lv, V. Stevanović, E. S. Toberer. *Chemistry of Materials* **2017**, *29*, 6 2494.

[21] B. Houston, R. E. Strakna, H. S. Belson. *Journal of Applied Physics* **1968**, *39*, 8 3913.

[22] J. W. Jaeken, S. Cottenier. *Computer Physics Communications* **2016**, *207* 445.

[23] K. Brugger. *Physical Review* **1965**, *137*, 6A A1826.

[24] D. C. Wallace. *Thermodynamics of Crystals*. John Wiley and Sons, Inc., New York, **1972**.

[25] T. Ungár. *Scripta Materialia* **2004**, *51*, 8 SPEC. ISS. 777.

[26] T. M. K. Thandavan, S. M. A. Gani, C. S. Wong, R. M. Nor. *Journal of Nondestructive Evaluation* **2015**, *34*, 2 1.

[27] A. Khorsand Zak, W. H. Abd. Majid, M. E. Abrishami, R. Yousefi. *Solid State Sciences* **2011**, *13*, 1 251.

[28] V. K. Pecharsky, P. Y. Zavalij. *Fundamentals of Powder Diffraction and Structural Characterization of Materials*. New York, New York, 2nd edition, **2009**.

[29] J. Hirth, J. Lothe. *Theory of Dislocations*. Malabar, Florida, 2nd edition, **1982**.

[30] M. Li, Z. Ding, Q. Meng, J. Zhou, Y. Zhu, H. Liu, M. S. Dresselhaus, G. Chen. *Nano Letters* **2017**, *17*, 3 1587.

[31] C. Zener. *Acta Crystallographica* **1949**, *2*, 3 163.

[32] A. Granato, K. Lücke. *Journal of Applied Physics* **1956**, *27*, 6 583.

[33] A. Maurel, V. Pagneux, F. Barra, F. Lund. *Physical Review B - Condensed Matter and Materials Physics* **2005**, *72*, 17 1.

[34] P. Klemens. In *Solid State Physics*, volume 7, 1–98. **1958**.

[35] A. Gibin, G. Devyatykh, A. Gusev, R. Kremer, M. Cardona, H.-J. Pohl. *Solid State Communications* **2005**, *133*, 9 569.

[36] T. Claudio, N. Stein, D. G. Stroppa, B. Klobes, M. M. Koza, P. Kudejova, N. Petermann, H. Wiggers, G. Schierning, R. P. Hermann. *Phys. Chem. Chem. Phys.* **2014**, *16*, 47 25701.

[37] C. J. Glassbrenner, G. a. Slack. *Physical Review* **1964**, *134*, 4A.

[38] X.-K. Wang, I. Veremchuk, M. Bobnar, J.-T. Zhao, Y. Grin. *Inorganic Chemistry Frontiers* **2016**, *3*, 9 1152.

[39] R. Hanus, A. Garg, G. J. Snyder. *Communications Physics* **2018**, *1*, 1 78.

[40] M. T. Agne, R. Hanus, G. J. Snyder. *Energy and Environmental Science* **2018**, *11*, 3 609.

[41] P. M. Kibasomba, S. Dhlamini, M. Maaza, C.-p. Liu, M. M. Rashad, D. A. Rayan, B. W. Mwakikunga. *Results in Physics* **2018**, *9* 628.

[42] G. Gouadec, P. Colomban. *Progress in Crystal Growth and Characterization of Materials* **2007**, *53*, 1 1.

[43] Y. Zhang, X. Ke, C. Chen, J. Yang, P. R. Kent. *Physical Review B - Condensed Matter and Materials Physics* **2009**, *80*, 2 1.

[44] R. M. Murphy, É. D. Murray, S. Fahy, I. Savić. *Physical Review B* **2016**, *93*, 10 1.

[45] G. Rogl, D. Setman, E. Schafler, J. Horky, M. Kerber, M. Zehetbauer, M. Falmbigl, P. Rogl, E. Royanian, E. Bauer. *Acta Materialia* **2012**, *60*, 5 2146.

[46] L. P. Hu, X. H. Liu, H. H. Xie, J. J. Shen, T. J. Zhu, X. B. Zhao. *Acta Materialia* **2012**, *60*, 11 4431.

[47] H.-S. Kim, S. D. Kang, Y. Tang, R. Hanus, G. Jeffrey Snyder. *Mater. Horiz.* **2016**, *3*, 3 234.

[48] T. Claudio, N. Stein, N. Petermann, D. G. Stroppa, M. M. Koza, H. Wiggers, B. Klobes, G. Schierning, R. P. Hermann. *Physica Status Solidi (A) Applications and Materials Science* **2016**, *213*, 3 515.

[49] B. Klobes, D. Bessas, F. Juranyi, H. Görlitz, V. Pacheco, R. P. Hermann. *Physica Status Solidi - Rapid Research Letters* **2015**, *9*, 1 57.

[50] F. Kargar, E. H. Penilla, E. Aytan, J. S. Lewis, J. E. Garay, A. A. Balandin. *Applied Physics Letters* **2018**, *112*, 19 191902.

[51] C. Mathioudakis, P. Kelires. *Journal of Non-Crystalline Solids* **2000**, *266-269* 161.

[52] D. Oleszak, P. H. Shingu. *Journal of Applied Physics* **1996**, *79*, 6 2975.

[53] B. H. Toby, R. B. Von Dreele. *Journal of Applied Crystallography* **2013**, *46*, 2 544.

[54] S. Christensen, N. Bindzus, M. Sist, M. Takata, B. B. Iversen. *Phys. Chem. Chem. Phys.* **2016**, *18*, 23 15874.

[55] R. Truell, C. Elbaum, B. B. Chick. *Ultrasonic Methods in Solid State Physics*. Academic Press Inc., New York, New York, **1969**.

[56] O. L. Anderson. *J. Phys. Chem. Solids* **1963**, *24* 909.

[57] E112-13, Standard Test Method for Determining Average Grain Size. Standard, American Society for Testing and Materials, West Conshohocken, PA, **2013**.

[58] Z. Wang, J. E. Alaniz, W. Jang, J. E. Garay, C. Dames. *Nano Letters* **2011**, *11*, 6 2206.

[59] B. Abeles. *Physical Review* **1963**, *131*, 5 1906.

[60] S. K. Bux, R. G. Blair, P. K. Gogna, H. Lee, G. Chen, M. S. Dresselhaus, R. B. Kaner, J. P. Fleurial. *Advanced Functional Materials* **2009**, *19*, 15 2445.